



## Promoted self-construction of $\beta$ -NiOOH in amorphous high entropy electrocatalysts for the oxygen evolution reaction

Mei Han<sup>a</sup>, Changhong Wang<sup>b</sup>, Jun Zhong<sup>c</sup>, Jingrui Han<sup>a</sup>, Ning Wang<sup>a,d</sup>, Ali Seifitokaldani<sup>e</sup>, Yifu Yu<sup>b</sup>, Yongchang Liu<sup>a,\*</sup>, Xuhui Sun<sup>c,\*</sup>, Alberto Vomiero<sup>f,g,\*\*</sup>, Hongyan Liang<sup>a,\*</sup>

<sup>a</sup> School of Materials Science and Engineering, Tianjin University, Tianjin 300350, China

<sup>b</sup> Institute of Molecular Plus, Tianjin University, Tianjin 300072, China

<sup>c</sup> Institute of Functional Nano and Soft Materials (FUNSOM), Soochow University, Suzhou 215123, China

<sup>d</sup> Department of Electrical and Computer Engineering, University of Toronto, 35 St George Street, Toronto, ON M5S 1A4, Canada

<sup>e</sup> Department of Chemical Engineering, McGill University, Montreal H3A 0C5, Canada

<sup>f</sup> Division of Materials Science, Department of Engineering Sciences and Mathematics, Luleå University of Technology, 97187 Luleå, Sweden

<sup>g</sup> Department of Molecular Sciences and Nanosystems, Ca' Foscari University of Venice, 30172 Venezia Mestre, Italy



### ARTICLE INFO

#### Keywords:

High entropy catalysts  
Oxygen evolution reaction  
Self-construction of  $\beta$ -NiOOH intermediates  
Amorphous nanoporous structure

### ABSTRACT

The exploration of an efficient electrocatalyst for the oxygen evolution reaction (OER) is urgently required for sustainable renewable-energy conversion and storage. Due to the increased chemical complexity, multimetallic catalysts provide flexibility to alter their electronic and crystal structure to attain a superior intrinsic catalytic activity via synergistic effects, which is seldom accomplished using single metal catalysts. However, the high chemical complexity increases the difficulty to prepare elemental homogenous catalysts and reveal their synergistic effect during OER process, which further hinder the design of multimetallic catalysts. Here, high entropy concept is utilized to design an NiFeCoMnAl oxide with amorphous structure as OER catalyst. The direct evidence of active Ni sites is provided by the *operando* Raman measurements and Fe can modify oxygen intermediates binding energy on Ni sites. The X-ray photoelectron spectroscopy (XPS) and X-ray absorption spectroscopy (XAS) reveal that the incorporation of Mn can construct the electron-rich environment of active Ni center, and the relatively lower oxidation state of Ni facilitates the self-construction of  $\beta$ -NiOOH intermediates, which shows promoted OER activity as confirmed by density functional theory calculations. Doping Co can enhance the conductivity and doping Al leads to the formation of nanoporous structure through dealloying process, thus each component is essential for improving OER performance. The optimized NiFeCoMnAl catalyst exhibits an overpotential of 190 mV at 10 mA cm<sup>-2</sup> in 1 M KOH solution, much superior to the ternary and quaternary counterparts. This work sheds light on understanding the origin of high entropy catalysts' OER activity and thereby enables the rational design of multinary transition metallic catalysts.

### 1. Introduction

Developing new technologies to capture solar energy and exploring green energy to solve the fossil energy crisis and the greenhouse effect has attracted global concern [1,2]. Electrochemical oxygen evolution reaction (OER) is a crucial half reaction in renewable-energy conversion and storage technologies, because it provides electrons to drive, for instance, electrochemical reducing protons or carbon dioxide into fuels

[3,4]. A major issue with OER is its substantial overpotential caused by the sluggish kinetics, leading to insufficient overall energy conversion efficiency [5,6]. First row transition metal catalysts, such as Cr, Mn, Fe, Co, Ni, Cu, have emerged as potential candidates for OER due to their relatively high activities, earth abundance, and stability under alkaline conditions, but most unary catalysts show an inferior performance which impedes their industrial implementation [7,8]. Constructing multimetallic catalysts has been demonstrated as an effective approach

\* Corresponding authors.

\*\* Corresponding author at: Division of Materials Science, Department of Engineering Sciences and Mathematics, Luleå University of Technology, 97187 Luleå, Sweden.

E-mail addresses: [ycliu@tju.edu.cn](mailto:ycliu@tju.edu.cn) (Y. Liu), [sunxuhui@gmail.com](mailto:sunxuhui@gmail.com), [xhsun@suda.edu.cn](mailto:xhsun@suda.edu.cn) (X. Sun), [alberto.vomiero@ltu.se](mailto:alberto.vomiero@ltu.se) (A. Vomiero), [hongyan.liang@tju.edu.cn](mailto:hongyan.liang@tju.edu.cn) (H. Liang).

to enhance OER activity.

Recently appeared high entropy concept has been utilized to design multimetallic catalysts with attractive mechanical properties [9,10]. Incorporation of five or more components at equal or near-equal molecular ratios, high entropy metallic materials achieve unprecedented superior physicochemical properties imposed by various interactions among constituent species [10,11]. Three causes are generally hypothesized for the enhanced catalytic activity of high entropy materials. (i) High entropy mixture modulates the electronic structure which results in enhanced intrinsic catalytic activity. Catalyst's electronic configuration has a strong relationship with its binding ability towards reaction intermediates which further determines its activity [12]. The tailored elemental composition and ratio in a high entropy catalyst enable to provide a possibility of altering its position on volcano plots toward a higher catalytic activity [13]. (ii) High entropy mixture promotes the generation of catalytically active sites. Morphology engineering has been adopted to modify surface and construct interface, which leads to favorable active site exposure. For example, porous structures formed by dealloying process provided high surface area to facilitate mass diffusion and expose abundant active sites [14,15]. Moreover, the different atomic radius of each component in multimetallic materials may increase atomic disorder and introduce structural defects/lattice strain, which encourages active metal site generation [16,17]. (iii) Finally, high entropy mixture enhances the electrical conductivity. High electrical conductivity plays a significant role in electrocatalytic processes because it promotes electron transfer and thus improves energy conversion efficiency [18–20]. Suitable element doping in high entropy metallic materials increases conductivity of the host catalyst to accelerate OER kinetics [21,22]. Therefore, compared to unary metals and traditional alloys, high entropy materials with well-designed compositions have the potential to demonstrate an enhanced catalytic activity.

Although high entropy materials are expected to demonstrate great electrocatalytic properties, their catalytic performance is barely explored due to the difficulty of preparing elemental homogenous structure and unraveling the role of each element in the complex multicomponent systems [23]. Moreover, the selectivity of metallic components for high entropy catalysts is not arbitrary, the cost, abundance, catalytic activities and miscibility must be considered. Several transition metals have been widely chosen as components for OER catalysts. For example, NiFe and NiFeCo oxide/hydroxide catalysts have been utilized as the starting materials for the multimetallic catalyst's design. Although the active sites are still under debate, the self-constructed  $\beta$ -NiOOH intermediates under applied potentials have been proved to show higher OER activity [24]. Al is a widely used precursor, which was chemically etched and selectively removing Al can form nanoscale pores and lead to more exposed active sites [25]. Co is found to narrow the band gap of NiFe and enhance the electron transfer efficiency [18,26]. Limited by the vastly difference in physicochemical properties, only a few families of high entropy alloys have been reported.

Herein we introduce high entropy concept into metal oxide catalysts which are fabricated using a facile and scalable electrodeposition method. Binary NiFe, as a highly active OER catalyst, is chosen as starting components, then Co, Mn and Al are doped to investigate how composition tailoring affects the OER performance [27]. All elements distribute homogeneously in the amorphous structure. The *operando* Raman measurements indicate that Ni sites are the active sites, and introducing Mn can promote the formation of  $\beta$ -NiOOH intermediates through constructing electron-rich environment.  $\beta$ -NiOOH intermediates show higher OER activity as proved by the density functional theory (DFT) calculations [22,28]. The doping Co and high valent Mn can enhance the conductivity of catalysts. The doping Al is used as a sacrifice template to form nanoporous structure after dealloying in an alkaline solution, leading to increased electrochemical active surface areas. Compared to the crystalline structure, the amorphous structure facilities the self-construction of  $\beta$ -NiOOH phase and provides abundant

uncoordinated sites for promoted catalytic activities. Each component is essential for the rationally engineered electrical and structural properties of catalysts, and the intrinsic OER activity is enhanced as a result of synergistic effect. Finally, the optimized NiFeCoMnAl catalyst exhibits an overpotential of 190 mV at 10 mA cm<sup>-2</sup>, a Tafel slope of 47.62 mV dec<sup>-1</sup> and operation stability of 50 h in 1 M KOH solution. This work provides a convincing demonstration of high entropy materials as effective OER catalysts, a comprehensive understanding of multiple elements synergistic effect and a potential guide for compositional design of electrocatalysts.

## 2. Experimental section

### 2.1. Reagents and materials

Nickel-(II) chloride (NiCl<sub>2</sub>), Iron-(II) chloride (FeCl<sub>2</sub>), Cobaltous-(II) chloride (CoCl<sub>2</sub>), Manganese-(II) chloride (MnCl<sub>2</sub>), Aluminum-(III) chloride (AlCl<sub>3</sub>), Dimethyl sulfoxide (DMSO), Lithium perchlorate (LiClO<sub>4</sub>), Ethylenediamine (EDA), Potassium hydroxide (KOH ≥ 99.9%) were purchased from Sigma-Aldrich. Milli-Q ultrapure water (> 18 MΩ·cm) was used in all experiments.

### 2.2. Synthesis of catalysts

NiCl<sub>2</sub>, FeCl<sub>2</sub>, CoCl<sub>2</sub>, MnCl<sub>2</sub> and AlCl<sub>3</sub> were dehydrated in vacuum. DMSO was dehydrated with 4A molecular sieves and distilled at reduced pressure to remove impurities. A three-electrode system was used to conduct electrodeposition experiment in DMSO-LiClO<sub>4</sub> electrolyte. The carbon paper was used as the working electrode with 0.25 cm<sup>2</sup> exposing area, the platinum foil was used as the counter electrode, and the saturated calomel electrode (SCE) was used as the reference electrode. NiCl<sub>2</sub>, FeCl<sub>2</sub>, CoCl<sub>2</sub>, MnCl<sub>2</sub>, AlCl<sub>3</sub>, LiClO<sub>4</sub> and EDA were dissolved in DMSO to form electrolyte (0.01 mol L<sup>-1</sup> NiCl<sub>2</sub>, 0.01 mol L<sup>-1</sup> FeCl<sub>2</sub>, 0.01 mol L<sup>-1</sup> CoCl<sub>2</sub>, 0.02 mol L<sup>-1</sup> MnCl<sub>2</sub>, 0.03 mol L<sup>-1</sup> AlCl<sub>3</sub>, 0.1 mol L<sup>-1</sup> LiClO<sub>4</sub>). Electrodeposition potential and time were –2.8 V (vs. SCE) and 30 min, respectively. NiFe, NiFeAl and NiFeCoAl were prepared following similar process with varied precursor compositions. The deposited electrode was soaked in 1.0 M KOH solution for 1 h to remove Al for nanoporous structure formation.

### 2.3. Physicochemical characterization

The morphologies of the synthesized catalysts were characterized by field-emission scanning electron microscopy (SEM) (Hitachi S-4800) and transmission electron microscopy (TEM) (JEM-2100F). The crystal structure, elemental distribution and composition were examined by powder X-ray diffraction (XRD) (Bruker D8), energy-dispersive X-ray spectroscopy (EDS) and inductively coupled plasma optical emission spectrometry (ICP-OES). The chemical states and surface composition information were analyzed by X-Ray photoelectron spectroscopy (XPS) (Thermo ESCALAB 250XI) and ex-situ X-ray absorption spectroscopy (XAS) (Beamline 11B of Shanghai Synchrotron Radiation Facility. All the samples were measured in fluorescent mode).

### 2.4. Electrochemical measurements

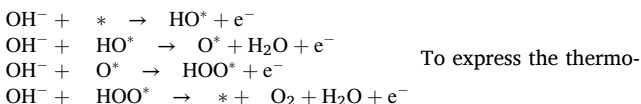
The electrochemical experiments were carried out with a standard three-electrode system connected to the electrochemical workstation (Autolab PGSTAT302N). The working electrode was carbon paper loaded with catalysts, the reference electrode was Ag/AgCl electrode, the counter electrode was Pt foil and the electrolyte was 1.0 M KOH and 0.5 M CO<sub>2</sub> saturated KHCO<sub>3</sub>. All measured potentials against the Ag/AgCl reference were converted to a reversible hydrogen electrode (RHE) scale, according to the formula of  $E_{RHE} = E_{Ag/AgCl} + 0.059 \times pH + 0.197$  V. Linear sweep voltammetry (LSV) was used to evaluate the catalytic activity. Before sweep, 20 cycles of cyclic voltammetry (CV)

measurements were performed at 50 mV s<sup>-1</sup> to activate the surface. The polarization curves were collected by performing LSV at a scan rate of 1 mV s<sup>-1</sup>. Tafel slopes were derived through plotting overpotential against log (current density) from the linear region of the LSV polarization curves. The value was calculated following the Tafel equation of  $\eta = b \times \log j + a$ , where  $\eta$  is the overpotential,  $b$  is the Tafel slope and  $j$  is the current density. Electrochemical impedance spectroscopy (EIS) measurements were carried out in a static solution at a potential of 1.5 V vs. RHE, with a frequency range from 0.1 Hz to 100 kHz. The steady-state activity was evaluated by chronopotentiometry measurements. The electrochemical double-layer capacitance ( $C_{dl}$ ) was performed to determine the electrochemical active surface area (ECSA). CV scans were carried out at a potential window of 0.87–0.99 V (vs. RHE) at different scan rates of 20, 40, 60, 80 and 100 mV s<sup>-1</sup>.  $C_{dl}$  value was obtained by plotting  $\Delta j = (j_{charge} - j_{off\ charge})$  at 0.93 V (vs. RHE) against the scan rates, and the linear slope is twice the  $C_{dl}$  value. ECSA was estimated following the equation:  $ECSA = C_{dl}/C_s$ , where  $C_s$  is 0.040 mF cm<sup>-2</sup>.

## 2.5. Theoretical calculation details

DFT calculations with a plane-wave basis were performed as implemented in Vienna ab initio Simulation Package (VASP) [29]. Projector augmented wave (PAW) pseudopotentials were used [30]. The exchange-correlation contributions to the total energy were estimated by the generalized gradient approximation (GGA) with Perdew-Burke-Ernzerhof (PBE) form [31]. The Hubbard U approach (DFT + U) was adopted to better describe the on-site Coulomb correlation of the localized 3d electrons for transition metals Ni with U -  $J = 3.4$  eV [32,33]. An empirical dispersion corrected DFT method (DFT-D3) was carried out to reasonably describe the weak long-distance van der Waals (vdWs) effects [34]. A kinetic-energy cutoff of 500 eV was used. During geometry optimizations, the maximum force on each atom was less than 0.05 eV/Å. The total energy convergence criterion was set as  $10^{-4}$  eV. Spin polarization was considered in all calculations.

The  $\beta$ -NiOOH and  $\gamma$ -NiOOH slabs were modeled by one (001) and (01-12) layer with edge Ni exposed, respectively. A vacuum layer of 15 Å was adopted along the c direction to avoid periodic image interactions. The Brillouin zone was sampled by k-point meshes of  $8 \times 2 \times 1$  and  $7 \times 3 \times 1$  for  $\beta$ -NiOOH and  $\gamma$ -NiOOH, respectively. For structural relaxation, the bottom atomic layer was fixed and all other atoms and adsorbates were fully relaxed. The OER under alkaline condition consists of four elementary reaction steps, each involving an electron transfer to the electrode.



chemistry of the sub-reactions of OER, the computational hydrogen electrode (CHE) model proposed by Nørskov and co-workers was used [35]. The reaction free energy change of each step was calculated using the following equation:

$$\Delta G_i = \Delta E_i + \Delta ZPE_i - T\Delta S_i \quad (5)$$

where  $i = 1, 2, 3, 4$  correspond to each step in OER.  $\Delta E$  is the reaction energy,  $\Delta ZPE$  is the change of zero-point energy,  $T$  (298.15 K) is temperature,  $\Delta S$  is the difference in entropy.

The theoretical overpotential was given as follows:

$$\eta = \frac{\text{Max}[\Delta G_i]}{e} - 1.23\text{V} \quad (6)$$

## 3. Results and discussion

### 3.1. Synthesis and characterization of the NiFeCoMnAl oxide

The nanoporous NiFeCoMnAl oxide was synthesized on carbon paper via electrochemical deposition followed by dealloying technique, as shown in the schematic of Fig. 1 and the detailed description incorporated in the Experimental Section. The morphology, crystalline structure and elemental distribution of the synthesized NiFeCoMnAl are shown in Fig. 2. The SEM and TEM images revealed that the catalysts were successfully deposited on carbon paper. Compared to the images of carbon paper before and after electrodeposition in Fig. S1, S2 and Fig. 2a, it is apparent that a layer of dense catalysts uniformly covers the surface of carbon fiber, leaving no exposed carbon surface. Electrodeposition creates a strong binding between the catalyst and substrate (i.e. carbon paper, Ni mesh or foam, glassy carbon, etc.) which makes it more stable under the OER condition with vigorous gas evolution compared to electrodes prepared through sticking catalyst powders to substrate via polymeric binders. XRD was used to identify the crystal structure of NiFeCoMnAl oxide. Fig. 2c shows no significant Bragg reflection of the freshly prepared sample, indicating the poor crystallinity of the deposited catalyst. This result is consistent with the amorphous structure revealed by TEM images without clear lattice fringes in Fig. 2b, e, f, and selected area electron diffraction (SAED) pattern with diffuse rings inserted in Fig. 2b.

The deposited electrode was soaked in 1.0 M KOH solution for 1 h before the OER to remove Al and create a nanoporous structure as shown in Fig. 2d and e. After dealloying process, Al was dissolved in the solution which was further confirmed by elemental analysis through the ICP-OES, as shown in Table S1. Fig. 2g demonstrates the atomic distribution of etched NiFeCoMnAl—mapped by the EDS elemental mapping—and reveals that residual Al element is extremely rare and homogeneously mixed with other elements (Ni, Fe, Co, Mn, O). No obviously elemental aggregation or segregation was observed. The EDS results of other compositions are shown in Fig. S3, and the elemental ratio was close to that in the starting precursors. These results confirm that the electrodeposition method can successfully incorporate multiple metallic components into one system, and keep precursors' initial stoichiometry in the final product. Thus, through the electrodeposition method catalysts can be synthesized with desired atomic ratios simply by adjusting the stoichiometry of precursors. For comparison, crystalline NiFeCoMnAl was prepared through annealing the amorphous structure in the air at 400 °C. The XRD pattern in Fig. 2c confirmed the formation of highly crystalline products with Ni<sub>2</sub>O<sub>3</sub> phase (JCPDS 20-0781) and MnFe<sub>2</sub>O<sub>4</sub> phase (JCPDS 10-0319). HRTEM and EDS elemental mapping in Fig. S4 reveals the crystalline structure and distribution of five elements in the annealed material. Moreover, these crystalline NiFeCoMnAl oxides show slight particle coarsening after the annealing process, offering an ideal model to compare the catalytic performance with amorphous catalysts.

To analyze the surface chemical states and confirm the electronic interactions of the high entropy materials, the XPS was carried out on NiFeAl, NiFeCoAl and NiFeCoMnAl catalysts. The survey spectra in Fig. S5 demonstrate the presence of Al, Ni, Fe, Co, Mn, O elements, which are consistent with EDS results. As shown in the high-resolution XPS spectrum in Fig. 3a, Ni 2p contains two obvious peaks at 856.1 eV (Ni 2p<sub>3/2</sub>) and 874.1 eV (Ni 2p<sub>1/2</sub>), indicating the presence of Ni<sup>2+</sup> state [28]. Compared to NiFeAl, both Ni<sup>2+</sup> 2p peaks for NiFeCoAl and NiFeCoMnAl are shifted by 0.2 eV and 0.8 eV toward the lower energy direction, respectively. In Fig. 3b, the signals of Fe 2p<sub>3/2</sub> (712.5 eV) and Fe 2p<sub>1/2</sub> (725.2 eV) are assigned to Fe<sup>3+</sup> and Fe<sup>2+</sup>, which show negative shifts of 0.7 eV after CoMn-doping [28]. A 0.5 eV shift of

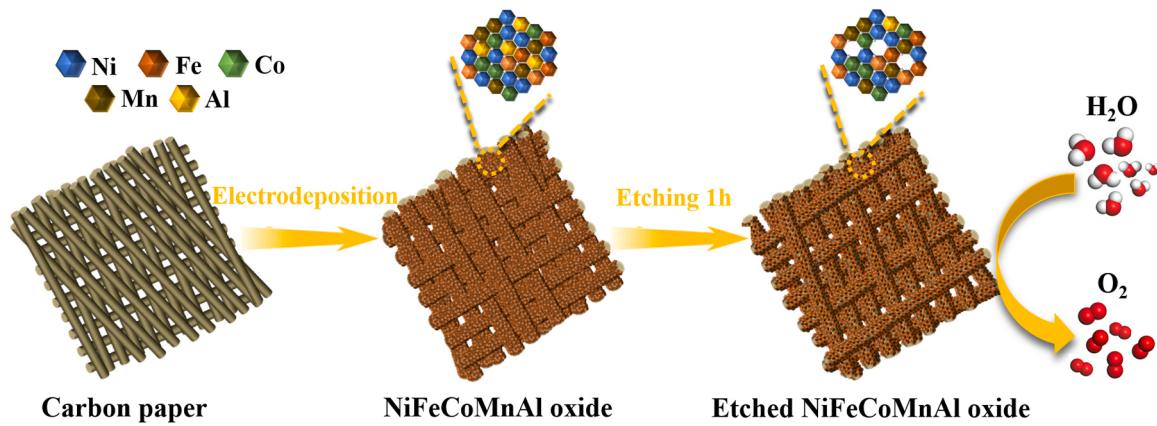


Fig. 1. Schematic illustration of the synthetic procedures for nanoporous NiFeCoMnAl oxide grown on carbon paper.

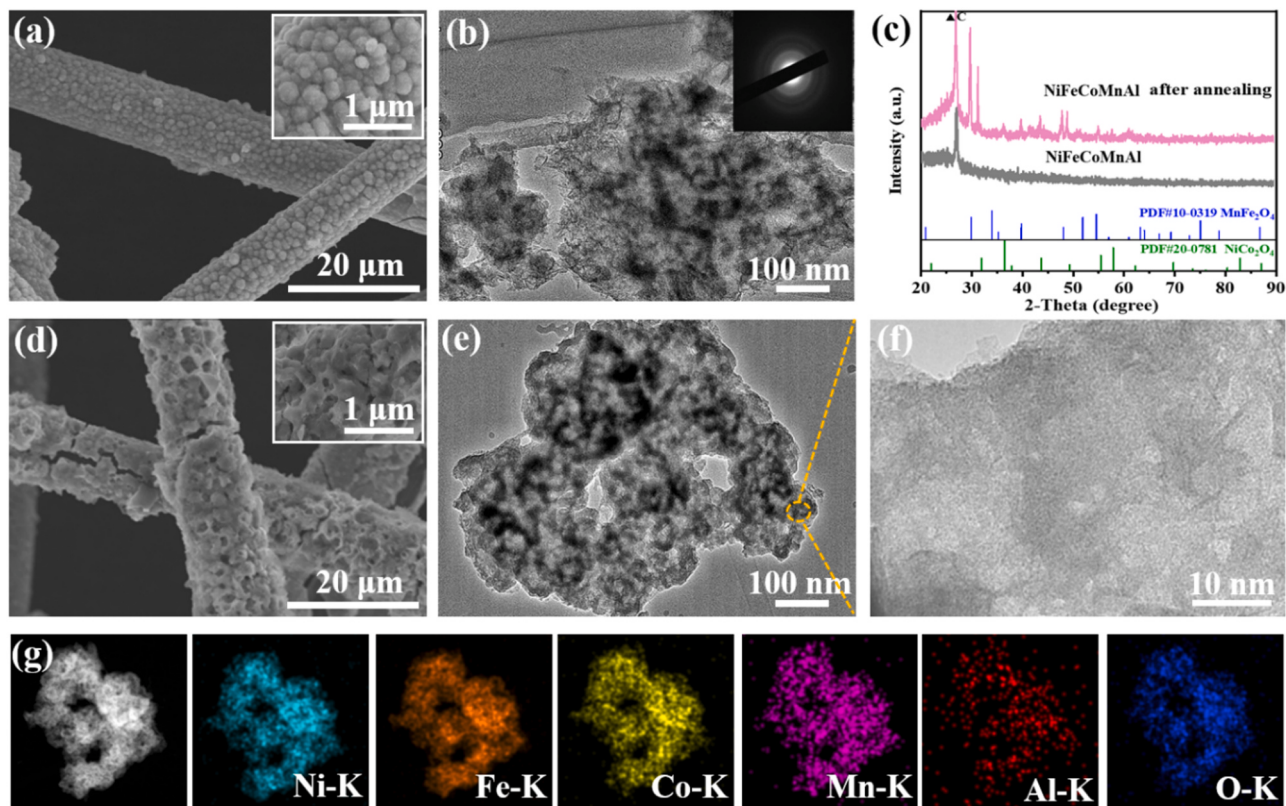
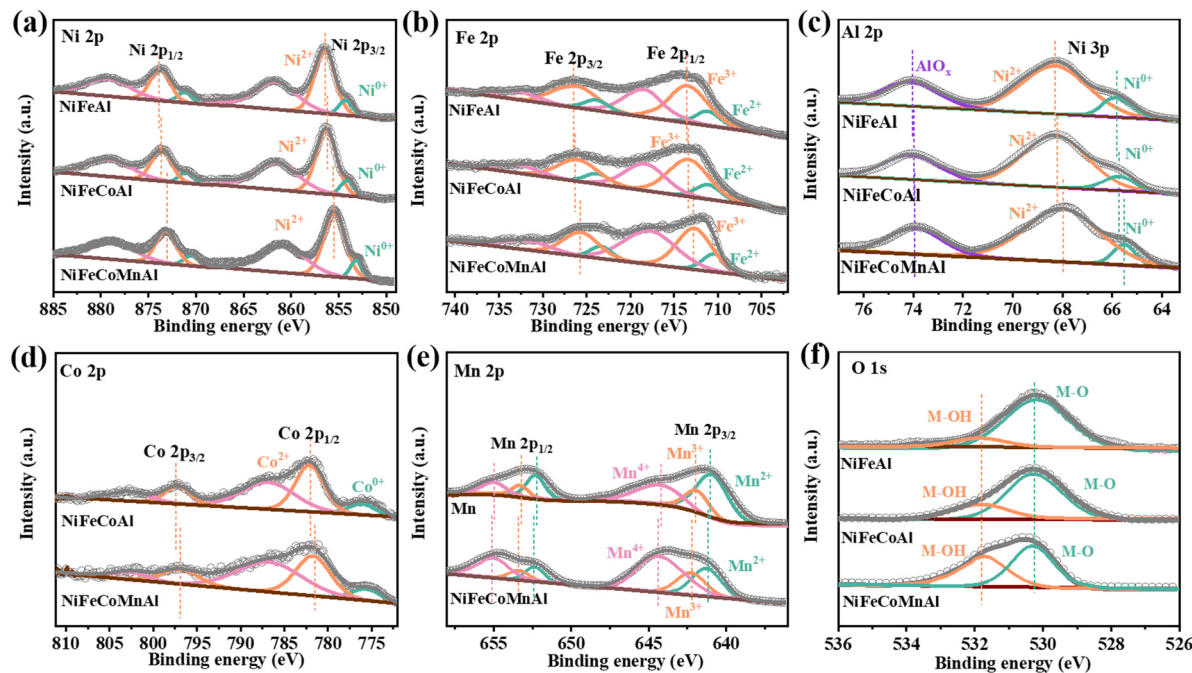


Fig. 2. Characterization of catalysts. The SEM and TEM images of NiFeCoMnAl before (a,b) and after (d,e) soaking in 1.0 M KOH, with insets displaying higher magnification images and SAED pattern. (c) XRD pattern of NiFeCoMnAl before and after annealing at 400 °C. (f) HRTEM image and (g) STEM image and corresponding EDS elemental mapping of Ni, Fe, Co, Mn, Al, O for etched NiFeCoMnAl.

Co 2p<sub>3/2</sub> (781.7 eV) and Co 2p<sub>1/2</sub> (797.7 eV) to lower energy was also observed with the incorporation of Mn, as shown in Fig. 3d. These results show that after Mn<sup>2+</sup> doping, the obvious negative shifts in binding energy peaks of Ni<sup>2+</sup>, Fe<sup>3+</sup>, Co<sup>2+</sup> happen, illustrating the electron transfer from Mn<sup>2+</sup> to Ni<sup>2+</sup>, Fe<sup>3+</sup> and Co<sup>2+</sup>. In Fig. 3e, Mn 2p<sub>3/2</sub> peak is deconvoluted into three components, which are ascribed as Mn<sup>2+</sup> at 641.1 eV, Mn<sup>3+</sup> at 642.2 eV and Mn<sup>4+</sup> at 644.3 eV, respectively [22,28]. Compared to single component Mn catalyst deposited by the same procedure, all Mn 2p<sub>3/2</sub> peaks showed slightly positive shifts towards higher binding energy with increased high-valent Mn<sup>4+</sup> content in NiFeCoMnAl, further indicating its role as electron donor. The reason is that the electronegativity of Mn<sup>2+</sup> is lower than those of Ni<sup>2+</sup>, Fe<sup>3+</sup> and Co<sup>2+</sup> leading to a weaker ability to attract electrons, thus electrons

transfer from Mn<sup>2+</sup> to Ni<sup>2+</sup>, Fe<sup>3+</sup> and Co<sup>2+</sup> happens. In this case, the electron density around the electron acceptors increased, which is beneficial for electrocatalysis [28]. Moreover, the existence of Mn<sup>4+</sup> in NiFeCoMnAl might accelerate the electron transport process and improve the conductivity [36].

In addition, the high-resolution XPS spectrum exhibited in Fig. 3c shows the Al 2p spectrum at ~74.0 eV which can be assigned to Al<sub>2</sub>O. After Co-doping and Mn-doping, Al 2p peak does not show obvious shifts, indicating an unaffected chemical state. Similarly, when Al was doped into NiFeCoMn, the XPS of Ni 2p, Fe 2p, Co 2p, Mn 2p in Fig. S6 showed no significant change, suggesting the negligible influence of Al towards other elements' electronic structure modification. Fig. 3f compared the binding energy evolution of O sites for NiFeAl, NiFeCoAl,



**Fig. 3.** The XPS analysis of non-etched catalysts (NiFeAl, NiFeCoAl and NiFeCoMnAl) in the (a) Ni 2p, (b) Fe 2p, (c) Al 2p, (d) Co 2p, (e) Mn 2p and (f) O 1s binding energy region.

NiFeCoMnAl. The O1s spectra were deconvoluted into two characteristic peaks of metal-O (530.4 eV) and metal-OH group (531.8 eV), respectively [22]. The metal-O bond is the dominant component in NiFeAl and NiFeCoAl. Accompanying the introduction of Co and Mn sites, more -OH is required to coordinate with metallic sites, leading to more M-OH bonds in NiFeCoMnAl [37]. Moreover, the Co doping is reported to change the electronic structure around Ni, and improve the

conductivity [18,26]. In summary, in NiFe-based catalysts, the doped Mn<sup>2+</sup> donates electrons to other elements, and thus provides electron-rich environment to lower their oxidation states [22]. Furthermore, the formation of high-valent Mn<sup>4+</sup> in NiFeCoMnAl enhances its electrical conductivity and improves energy conversion efficiency [21]. The doped Co shows mainly an effect on enhanced conductivity [18,26]. The doped Al atoms do not have significant effects

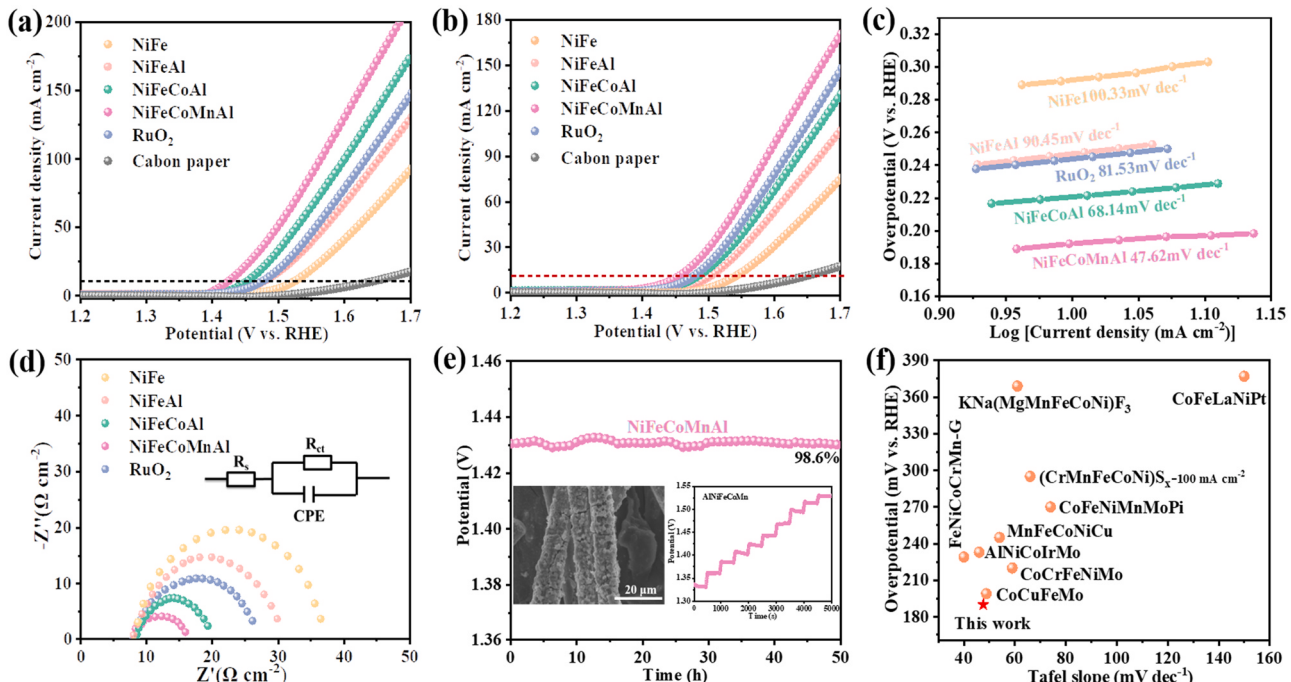


**Fig. 4.** Characterization of the electrochemical OER activities of the catalysts in 1.0 M KOH. (a, b) LSV polarization curves of catalysts before and after annealing; (c) Corresponding Tafel plots of catalysts; (d) Nyquist plots measured at open circuit potential by EIS; (e) Chronopotentiometry curves obtained with NiFeCoMnAl at a constant current density of 10 mA cm<sup>-2</sup>, with insets displaying the SEM image after long time reaction (left) and the multi-current process for NiFeCoMnAl (right); (f) Comparison of the overpotential and Tafel slope with other recently reported high entropy OER electrocatalysts.

on other elements' electronic structure, but the dissolution of Al in alkaline solution leads to the construction of nanoporous structure with abundance defects, which also favors the improvement of OER performance [38].

### 3.2. OER performance of the NiFeCoMnAl catalyst

In this work, the catalysts for electrochemical experiments under alkaline condition are all pre-treated by being immersed in 1.0 M KOH for 1 h. The differences in electrochemical performance and element content of catalysts before and after pretreatment were shown in Fig. S7. To evaluate the OER performance of NiFeCoMnAl, the LSV was carried out in 1 M KOH electrolyte, and it was found that  $\text{Ni}^{2+}/\text{Ni}^{3+}$  redox peak [39,40] on LSV curves was quiet weak (Fig. S8). As shown in Fig. 4a, a current density of  $10 \text{ mA cm}^{-2}$  obtained at an overpotential of 190 mV for optimized NiFeCoMnAl, which is the lowest among all reference materials (225 mV for NiFeCoAl, 250 mV for NiFeAl, 290 mV for NiFe, 245 mV for RuO<sub>2</sub>), and its performance is comparable to or better than previously reported high-entropy catalysts as summarized in Fig. 4f [41–49]. After annealing in air at 400 °C, NiFeCoMnAl shows the overpotential of 220 mV at a current density of  $10 \text{ mA cm}^{-2}$ , as shown in Fig. 4b (250 mV for NiFeCoAl, 280 mV for NiFeAl, 315 mV for NiFe), indicating the favorable OER performance for the amorphous metal oxide catalyst. The reaction kinetics was evaluated by the Tafel slope (Fig. 4c). The amorphous NiFeCoMnAl showed a small Tafel slope of 47.62 mV dec<sup>-1</sup>, which is much smaller than those of NiFeCoAl (68.14 mV dec<sup>-1</sup>), NiFeAl (90.45 mV dec<sup>-1</sup>) NiFe (100.33 mV dec<sup>-1</sup>) and RuO<sub>2</sub> (81.53 mV dec<sup>-1</sup>), indicating the fast reaction kinetics. To investigate the change of catalysts' conductivity, EIS measurements were carried out. The Nyquist plots in Fig. 4d show semicircular arcs, which were used to evaluate the charge transfer resistance ( $R_{ct}$ ). Compared with NiFe and NiFeAl, the NiFeCoAl shows a significantly decreased diameter, and this result confirmed that Co-doping can effectively enhance the conductivity. The lowest diameter was achieved from amorphous NiFeCoMnAl, demonstrating the fastest charge transfer and the highest conductivity resulting from both doped Co<sup>2+</sup> and Mn<sup>4+</sup>. The long-term stability of amorphous NiFeCoMnAl was demonstrated by chronopotentiometry at a current density of  $10 \text{ mA cm}^{-2}$  for over 50 h, as shown in Fig. 4e, which is further confirmed by the 1000 CV cycles measurement in Fig. S9 and multiple current steps of chronopotentiometry experiment and SEM image after OER operation in Fig. 4e.

The ECSA was evaluated by electrochemical capacitance measurement as shown in Fig. S10. The ECSA values were calculated to be  $340 \text{ cm}^2$ ,  $307.5 \text{ cm}^2$ ,  $290 \text{ cm}^2$ ,  $206.5 \text{ cm}^2$  for NiFeCoMnAl, NiFeCoAl, NiFeAl, NiFe, respectively. The ECSA value of NiFeCoMnAl is the highest, demonstrating the increased exposure of active sites. Nevertheless, the enlarged ECSA is not the main reason for the enhanced OER performance, which is confirmed by the normalized OER performance against the ECSA in Fig. S11. When the LSV curves are normalized against the ECSA, the NiFeCoMnAl electrode still exhibits the highest OER activity, indicating that the intrinsic OER activity of NiFeCoMnAl is higher than that of other counterparts. Meanwhile, the ECSA and normalized LSV curve of amorphous NiFeCoMnAl are greater than those of crystalline NiFeCoMnAl, indicating amorphous NiFeCoMnAl has better intrinsic OER activity than crystalline NiFeCoMnAl. The mass activities were also measured to further evaluate the intrinsic OER activity of these catalysts. The current was measured at an overpotential of 350 mV with a catalyst loading mass of  $0.35 \text{ mg cm}^{-2}$ . As shown in Fig. S12, the mass activity of NiFeCoMnAl catalyst is  $450 \text{ A g}^{-1}$ , which is higher than that of NiFeCoAl ( $350 \text{ A g}^{-1}$ ), NiFeAl ( $245 \text{ A g}^{-1}$ ) and NiFe ( $155 \text{ A g}^{-1}$ ). The turnover frequency (TOF) could be used to further compare the intrinsic activity of NiFeCoMnAl with that of other catalysts, as shown in Fig. S13. The TOF data for NiFeCoMnAl was calculated to be  $0.526 \text{ mol O}_2 \text{ s}^{-1}$  at overpotential of 350 mV, much higher than that of NiFeCo ( $0.170 \text{ mol O}_2 \text{ s}^{-1}$ ,  $Z = 350 \text{ mV}$ ) [50], NiFeMn

( $0.138 \text{ mol O}_2 \text{ s}^{-1}$ ,  $Z = 300 \text{ mV}$ ) [51] and NiFeAl ( $0.170 \text{ mol O}_2 \text{ s}^{-1}$ ,  $Z = 350 \text{ mV}$ ) [22]. In addition, we investigated OER performance of these catalysts electrodeposited on Ni foam (Fig. S14). We observed that the OER performance of all catalysts is further improved, and the NiFeCoMnAl oxide shows an overpotential of 300 mV at a current density of  $1000 \text{ mA cm}^{-2}$  with I-R correction.

After the OER operation, the NiFeCoMnAl catalyst was characterized by SEM, TEM, HRTEM, SAED and EDS elemental mapping, as shown in Fig. S15. No obvious morphology and component distribution change was observed, suggesting high stability of the NiFeCoMnAl catalyst. The valence states of the NiFeAl, NiFeCoAl, NiFeCoMnAl catalysts after the OER were investigated by XPS (Fig. S16). Compared with fresh electrodes, we observed that the valence states of Ni, Fe, Co, Mn increased after OER operation, demonstrating the higher oxidation states. For Al 2p, the peak position did not shift after OER, which is related to the unchanged chemical state. In addition, the signal of AlO<sub>x</sub> almost disappeared due to Al dissolution during dealloying process in alkaline solution, which favors the generation of defects and consequently promotes the OER. In addition, the O1s spectra were deconvoluted into three characteristic peaks of metal-O (530.4 eV), oxygen vacancies (531.2 eV) and metal-OH group (531.8 eV), respectively [22]. More oxygen vacancies generated in NiFeCoMnAl may further accelerate the OER kinetics [37]. Moreover, we also explored the OER performance of NiFeCoMnAl under acidic conditions and found that the performance was terrible (Fig. S17). The effect of electrodeposition time was also investigated. Those electrodes fabricated by longer or shorter electrodeposition time did not show excellent conductivity (Fig. S18).

Moreover, the OER performance of the NiFeCoMnAl under neutral condition was investigated. In 0.5 M CO<sub>2</sub> saturated KHCO<sub>3</sub> (pH = 7.1), the NiFeCoMnAl showed an overpotential of 390 mV, which is lower than that of NiFeCoAl (430 mV), NiFeAl (470 mV), NiFe (480 mV) and RuO<sub>2</sub> (415 mV), as shown in Fig. 5a. The reaction kinetics was evaluated by the Tafel slope in Fig. 5b. The NiFeCoMnAl shows a Tafel slope of 126.61 mV dec<sup>-1</sup>, which was smaller than that of other catalysts (NiFeCoAl, 163.52 mV dec<sup>-1</sup>; NiFeAl, 187.74 mV dec<sup>-1</sup>; NiFe, 194.17 mV dec<sup>-1</sup>; RuO<sub>2</sub>, 148.03 mV dec<sup>-1</sup>). The EIS measurements at 1.5 V (vs. RHE) were also performed (Fig. 5c). The small semicircle diameter of Nyquist plots of NiFeCoMnAl revealed a lower charge transfer resistance ( $R_{ct}$ ), indicating that charge transfer process is faster.

We noticed that Al element cannot be etched in 0.5 M CO<sub>2</sub> saturated KHCO<sub>3</sub>, therefore NiFeAl and NiFe showed comparable overpotentials, indicating nanoporous structure and defects caused by Al dissolution in alkaline environment play an important role to improve OER performance. Nevertheless, positive effects of Co and Mn doping on OER performance were observed in neutral condition, which is consistent with the results attained in alkaline condition. Moreover, the long-term stability was carried out at a constant current density of  $10 \text{ mA cm}^{-2}$  in neutral electrolyte for 60 h (Fig. 5d), validating the good stability of the NiFeCoMnAl under neutral condition. According to all these experimental results, NiFeCoMnAl catalyst demonstrates a lower overpotential, a smaller Tafel slope and a faster charge transfer rate than that of other control catalysts investigated here, which indicate its superior OER activity.

### 3.3. Mechanism investigation for the NiFeCoMnAl oxide in OER

To further understand the synergistic effect between Ni, Fe, Co and Mn, the time dependent *operando* Raman measurements were carried out as shown in Fig. 6 and Fig. S19. As shown in Fig. 6, the *operando* Raman spectra were recorded at applied potentials ranging from open circuit potential (OCP) to 0.8 V vs. Ag/AgCl. In OCP condition, the doublet peaks located at 400–600 cm<sup>-1</sup> represent the Ni-O stretches in oxide phase [52], and the peak located at ~680 cm<sup>-1</sup> is ascribed to Ni-O stretches in hydroxide phase [52]. Under OCP condition, the Raman spectrum of NiFeCoMnAl shows an obvious Ni-O signal at ~680 cm<sup>-1</sup>, indicating the higher ratio of hydroxide structures, which agrees well

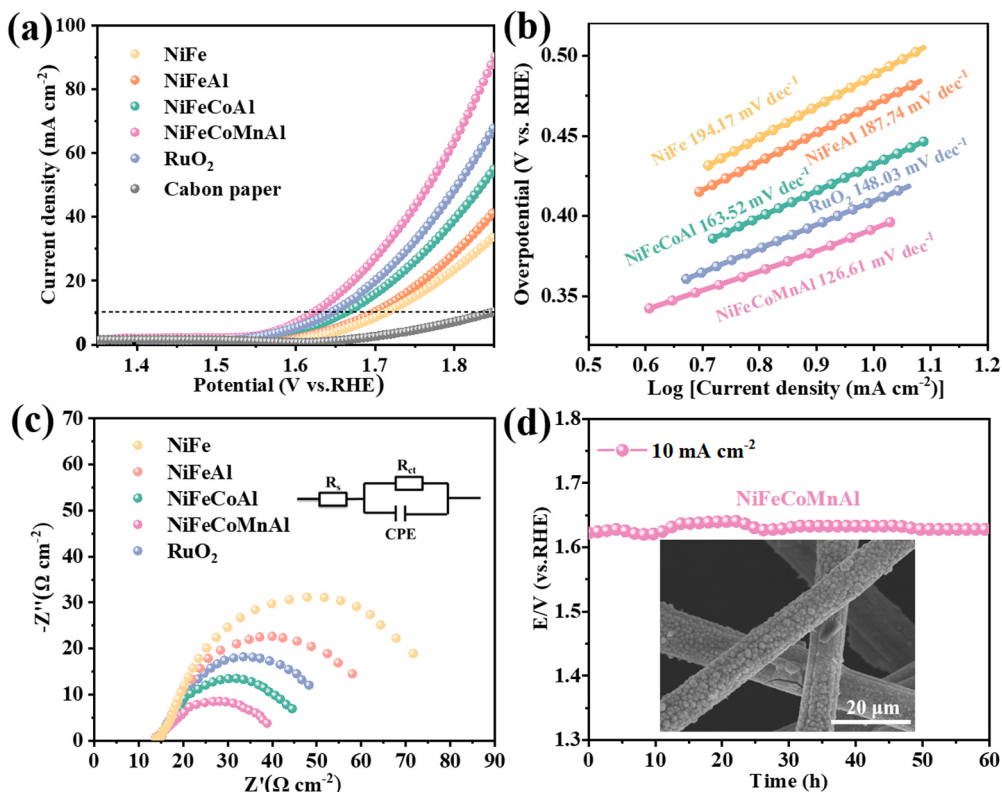


**Fig. 5.** Characterization of the electrochemical OER activities of the catalysts in 0.5 M  $\text{CO}_2$  saturated  $\text{KHCO}_3$ . (a) LSV polarization curves of NiFe, NiFeAl, NiFeCoAl, NiFeCoMnAl, RuO<sub>2</sub> and carbon paper and (b) corresponding Tafel plots of the catalysts; (c) Nyquist plots measured at open circuit potential by EIS; (d) Chronopotentiometry curve obtained with NiFeCoMnAl at a constant current density of  $10 \text{ mA cm}^{-2}$  and the SEM image of NiFeCoMnAl after long-term reaction.

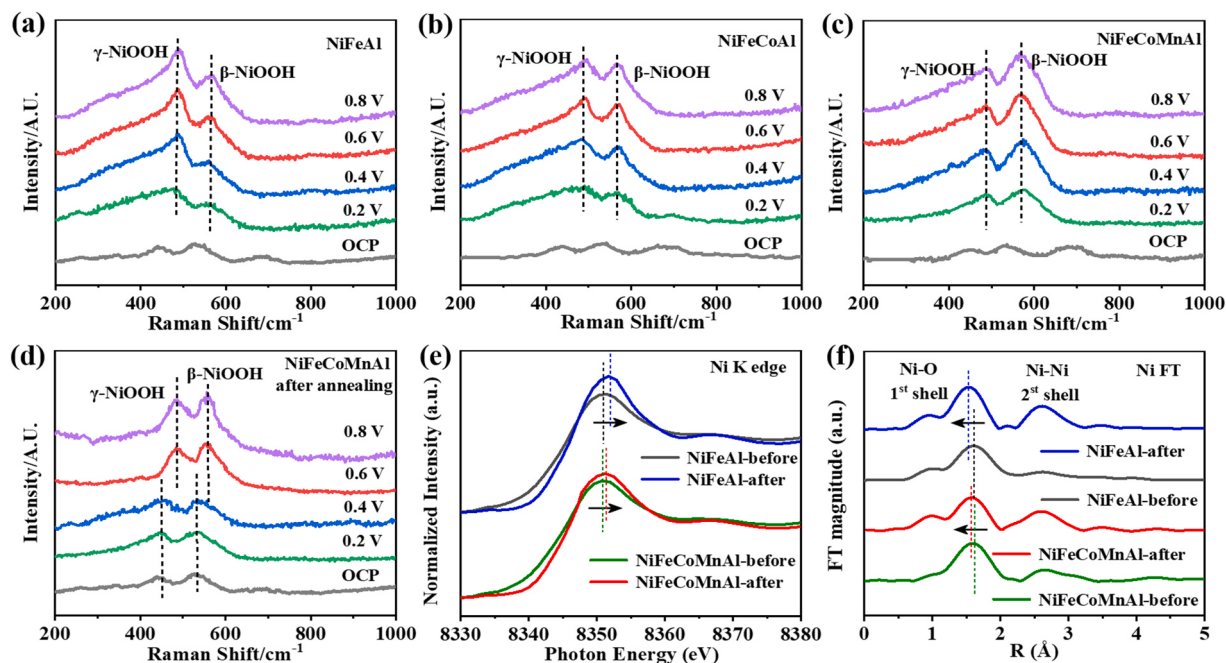


**Fig. 6.** The operando Raman spectra of the (a) NiFeAl, (b) NiFeCoAl, (c) NiFeCoMnAl and (d) NiFeCoMnAl-after annealing catalysts under various applied potentials; (e, f) The XANES and FT-EXAFS of NiFeAl and NiFeCoMnAl catalysts before and after OER at Ni K-edge.

with the XPS analysis of O 1s. Under applied potential, the doublet Ni-O peaks of nickel oxide phase red-shift, confirming the appearance of the NiOOH, a mixture of  $\gamma$ -NiOOH ( $\sim 475 \text{ cm}^{-1}$ ) and  $\beta$ -NiOOH ( $\sim 555 \text{ cm}^{-1}$ ) intermediates [53,54]. Thus, the Ni sites were the active sites in our

system and no other MOOH intermediates were observed. Noted that the ratio of two NiOOH intermediates varied with applied potentials and different compositions. For NiFeAl catalyst (Fig. 6a), the content of  $\gamma$ -NiOOH intermediates is higher than that of  $\beta$ -NiOOH. However, the

$\beta$ -NiOOH intermediates in NiFeCoMnAl are dominant, as shown in Fig. 6c and Fig. S19, which is quite different from that in NiFeAl (Fig. 6a) and NiFeCoAl (Fig. 6b). That reason might be that the Mn-doping provides electron-rich environment to lower the oxidation state of Ni, which facilitates the formation of  $\beta$ -NiOOH intermediate ( $Ni \leq +3$ ), rather than  $\gamma$ -NiOOH intermediate ( $Ni > +3$ ) [24]. To further compare the unique advantage of amorphous structure during the OER process, we also carried out the *operando* Raman operation for crystalline NiFeCoMnAl. As shown in Fig. 6d, the crystalline NiFeCoMnAl substantially retains the Ni-O structure and no NiOOH species were detected until the potential applied at 0.6 V. However, Ni-O in amorphous NiFeCoMnAl can evolve into NiOOH phase completely under a low applied potential of 0.2 V (Fig. 6c), demonstrating that the amorphous structure favors the formation of NiOOH.

The XAS was applied to understand the influence of Mn doping on the valence state of Ni in NiFeCoMnAl during the OER. The Ni K-edge X-ray absorption of near-edge spectroscopy (XANES) and extended X-ray absorption fine structure (EXAFS) spectra of NiFeAl and NiFeCoMnAl catalysts before and after OER were collected, as shown in Fig. 6e and f. Before OER operation, the white line peak of Ni K-edge in NiFeCoMnAl and NiFeAl show no significant difference. In EXAFS spectra of pristine sample, as shown in Fig. 6f, the peak at  $\sim 1.5$  Å can be assigned to the Ni-O bond of  $Ni(OH)_2$ , and the peak at  $\sim 2.6$  Å can be assigned to Ni-Ni bond between neighbor octahedral cages [24]. After OER operation, the Ni edge shifted toward a higher energy direction compared with the fresh electrodes, which suggested the appearance of the higher oxidation state of Ni. The peak shift in NiFeCoMnAl is smaller than that of NiFeAl, which is in agreement with the lower oxidation states of Ni in XPS results in Fig. S16. For EXAFS spectra, the peak position of Ni-O and Ni-Ni in both samples slightly shift towards the lower R direction, and the peak shift of NiFeAl is larger than that of NiFeCoMnAl, indicating the formation of shorter Ni-O bonds for NiFeAl catalyst. Compared with NiFeAl, NiFeCoMnAl has a lower oxidation state of Ni, which is consistent with the results of XANES and XPS.

Taken together, the pristine NiFeAl was dominated by metallic oxide phase, and NiFeCoMnAl contains more metallic hydroxides phase. Mn doping increased the content of  $Ni(OH)_2$  and reduced the valent states of Ni. During OER process, the lower oxidized states of Ni are easier to transfer into  $\beta$ -NiOOH intermediate ( $Ni \leq +3$ ), rather than  $\gamma$ -NiOOH intermediate ( $Ni > +3$ ). It is noticeable that previous report revealed the

$\beta$ -NiOOH intermediate exhibits a higher OER activity than that of  $\gamma$ -NiOOH intermediate, which might be the reason for the higher OER performance of NiFeCoMnAl [53,55]. To better understand the experimental results, DFT calculations were conducted to reveal the OER reaction free energy of each step over  $\beta$ -NiOOH and  $\gamma$ -NiOOH surfaces. The free energy landscape for each oxide intermediate (\*OH, \*O and \*OOH, where \* represents the active sites) is shown in Fig. 7. The detailed Gibbs free energy changes ( $\Delta G$ ) for each step were calculated at zero potentials versus RHE. The  $O^*$  formation is the potential limiting step (PLS) for both  $\beta$ -NiOOH and  $\gamma$ -NiOOH. The OER overpotential of 0.38 eV over  $\beta$ -NiOOH is much lower than that of  $\gamma$ -NiOOH (0.71 eV), which demonstrates that the OER activity should be  $\beta$ -NiOOH  $>$   $\gamma$ -NiOOH. This result is consistent with the experimental and the *operando* Raman results. Above all, the  $\beta$ -NiOOH can work as more active catalytic sites, boost OER catalytic activity and optimized adsorption of \*OH and \*O intermediates.

#### 4. Conclusions

In conclusion, electrodeposition method was used to fabricate high entropy materials with tailored compositions as efficient OER electrocatalysts. According to all these experimental results, NiFeCoMnAl catalyst demonstrates a lower overpotential of 190 mV at 10 mA cm<sup>-2</sup>, a smaller Tafel slope of 47.62 mV dec<sup>-1</sup> and a faster charge transfer rate than that of other control catalysts investigated here, which indicate its superior OER activity. The origin of the high OER activity could be attributed to the following factors: (i) the incorporation of Mn can construct electron-rich environment of active Ni centers, and the relatively lower oxidation state of Ni facilitates the self-construction of  $\beta$ -NiOOH intermediates resulting in promoted deprotonating step and lowers the required overpotential for the OER. (ii) The doped Co and the formation of  $Mn^{4+}$  can enhance conductivity, which helps the charge transfer process to boost the OER rate. (iii) Dealloying of Al can form nanoporous structure with abundant defects, promoting the generation and exposure of active sites. (iv) The amorphous structure facilities the self-construction of  $\beta$ -NiOOH phase and provides abundant uncoordinated sites for promoted catalytic activities. These findings suggest that designing multicomponent metallic catalysts is an effective avenue to promote electrocatalytic activity.

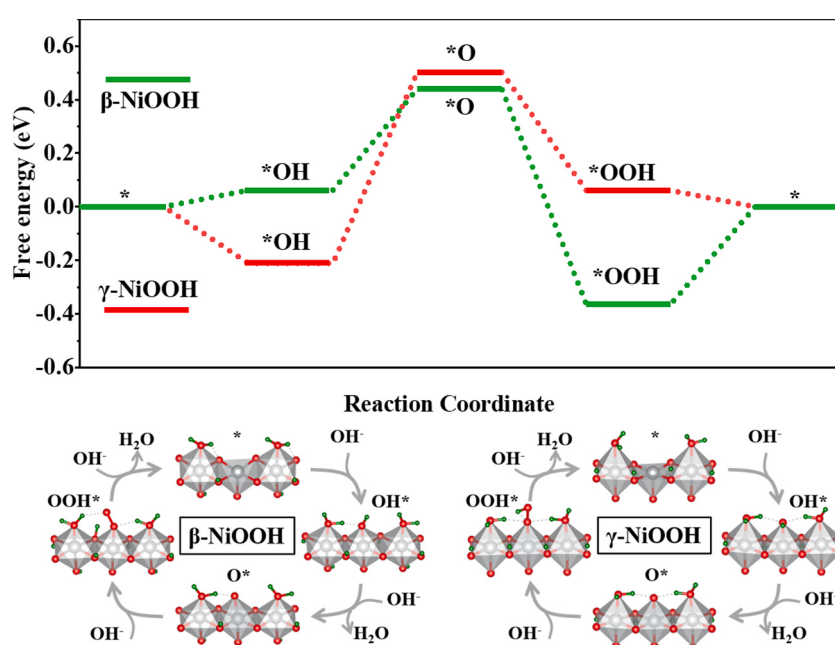


Fig. 7. Reaction energy diagram of water oxidation on  $\beta$ -NiOOH and  $\gamma$ -NiOOH models at different stages of the reaction.

## CRediT authorship contribution statement

**Mei Han** carried out the whole experiments and wrote the paper. **Changhong Wang** carried out the DFT simulations. **Jun Zhong** performed XAS measurements. **Jingrui Han, Ning Wang, Ali Seifitokaldani and Yifu Yu** conducted the characterizations and performed the results analysis. **Yongchang Liu, Xuhui Sun, Alberto Vomiero and Hongyan Liang** guided the whole project and revised the paper.

## Declaration of Competing Interest

The authors declare that they have no known competing financial interests or personal relationships that could have appeared to influence the work reported in this paper.

## Acknowledgments

This work was supported by the National Natural Science Foundation of China (NSFC No. 51771132). The authors thank Beamline 11B of Shanghai Synchrotron Radiation Facility for providing synchrotron beamtimes and technical supports.

## Appendix A. Supporting information

Supplementary data associated with this article can be found in the online version at [doi:10.1016/j.apcatb.2021.120764](https://doi.org/10.1016/j.apcatb.2021.120764).

## References

- [1] C. Chen, Y. Tu, Q. Lu, H. Lu, S. Zhang, Y. Zhou, J. Zhang, Z. Liu, Z. Kang, X. Feng, D. Chen, Hierarchical trimetallic Co-Ni-Fe oxides derived from core-shell structured metal-organic frameworks for highly efficient oxygen evolution reaction, *Appl. Catal. B Environ.* 287 (2021), 119953, <https://doi.org/10.1016/j.apcatb.2021.119953>.
- [2] C. Li, B. Zhang, Y. Li, S. Hao, X. Cao, G. Yang, J. Wu, Y. Huang, Self-assembled Cu-Ni bimetal oxide 3D in-plane epitaxial structures for highly efficient oxygen evolution reaction, *Appl. Catal. B Environ.* 244 (2019) 56–62, <https://doi.org/10.1016/j.apcatb.2018.11.046>.
- [3] B. Zhang, X.L. Zheng, O. Voznyy, R. Comin, M. Bajdich, M. Garcia-Melchor, L. Han, J.X. Xu, M. Liu, L.R. Zheng, F.P.G. de Arquer, C.T. Dinh, F.J. Fan, M. J. Yuan, E. Yassitepe, N. Chen, T. Regier, P.F. Liu, Y.H. Li, P. De Luna, A. Jammohamed, H.L.L. Xin, H.G. Yang, A. Vojvodic, E.H. Sargent, Homogeneously dispersed multimetal oxygen-evolving catalysts, *Science* 352 (2016) 333–337, <https://doi.org/10.1126/science.aaf1525>.
- [4] C. Huang, B. Zhang, Y. Wu, Q. Ruan, L. Liu, J. Su, Y. Tang, R. Liu, P.K. Chu, Experimental and theoretical investigation of reconstruction and active phases on honeycombed Ni<sub>3</sub>N-Co<sub>3</sub>N/C in water splitting, *Appl. Catal. B Environ.* 297 (2021), 120461, <https://doi.org/10.1016/j.apcatb.2021.120461>.
- [5] C.C. McCrory, S. Jung, J.C. Peters, T.F. Jaramillo, Benchmarking heterogeneous electrocatalysts for the oxygen evolution reaction, *J. Am. Chem. Soc.* 135 (2013) 16977–16987, <https://doi.org/10.1021/ja407115p>.
- [6] Q. Sun, B. Zhang, K. Song, Y. Guo, Y.A. Wang, E. Liu, F. He, Electronic reconfiguration of metal rhenium induced by strong metal-support interaction enhancing the hydrogen evolution reaction, *Adv. Mater. Interfaces* 8 (2021), 2100545, <https://doi.org/10.1002/admi.202100545>.
- [7] M. Han, N. Wang, B. Zhang, Y. Xia, J. Li, J. Han, K. Yao, C. Gao, C. He, Y. Liu, Z. Wang, A. Seifitokaldani, X. Sun, H. Liang, High-valent nickel promoted by atomically embedded copper for efficient water oxidation, *ACS Catal.* 10 (2020) 9725–9734, <https://doi.org/10.1021/acscatal.0c01733>.
- [8] L.G. He, P.Y. Cheng, C.C. Cheng, C.L. Huang, C.T. HSieh, S.Y. Lu, NixFeyCo<sub>6-x-y</sub>Mo<sub>6</sub>C cuboids as outstanding bifunctional electrocatalysts for overall water splitting, *Appl. Catal. B Environ.* 290 (2021), 120049, <https://doi.org/10.1016/j.apcatb.2021.120049>.
- [9] G. Fang, J.J. Gao, J. Lv, H.L. Jia, H.L. Li, W.H. Liu, G.Q. Xie, Z.H. Chen, Y. Huang, Q.H. Yuan, X.J. Liu, X. Lin, S.H. Sun, H.J. Qiu, Multi-component nanoporous alloy/(oxy)hydroxide for bifunctional oxygen electrocatalysis and rechargeable Zn-air batteries, *Appl. Catal. B Environ.* 268 (2020), 118431, <https://doi.org/10.1016/j.apcatb.2019.118431>.
- [10] H. Chen, K.C. Jie, C.J. Jafra, Z.Z. Yang, S.Y. Yao, M.M. Liu, Z.H. Zhang, J.X. Liu, M. F. Chi, J. Fu, S. Dai, An ultrastable heterostructured oxide catalyst based on high-entropy materials: a new strategy toward catalyst stabilization via synergistic interfacial interaction, *Appl. Catal. B Environ.* 276 (2020), 119155, <https://doi.org/10.1016/j.apcatb.2020.119155>.
- [11] Y.G. Yao, Z.N. Huang, P.F. Xie, S.D. Lacey, R.J. Jacob, H. Xie, F.J. Chen, A.M. Nie, T.C. Pu, M. Rehwoldt, D.W. Yu, M.R. Zachariah, C. Wang, R. Shahbazian-Yassar, J. Li, L.B. Hu, Carbothermal shock synthesis of high-entropy-alloy nanoparticles, *Science* 359 (2018) 1489–1494, <https://doi.org/10.1126/science.aan5412>.
- [12] T.A.A. Batchelor, J.K. Pedersen, S.H. Winther, I.E. Castelli, K.W. Jacobsen, J. Rossmeisl, High-entropy alloys as a discovery platform for electrocatalysis, *Joule* 3 (2019) 834–845, <https://doi.org/10.1016/j.joule.2018.12.015>.
- [13] H.J. Qiu, G. Fang, Y.R. Wen, P. Liu, G.Q. Xie, X.J. Liu, S.H. Sun, Nanoporous high-entropy alloys for highly stable and efficient catalysts, *J. Mater. Chem. A* 7 (2019) 6499–6506, <https://doi.org/10.1039/c9ta00505f>.
- [14] S. Chen, D. Huang, D. Liu, H. Sun, W. Yan, J. Wang, M. Dong, X. Tong, W. Fan, Hollow and porous NiCo<sub>2</sub>O<sub>4</sub> nanospheres for enhanced methanol oxidation reaction and oxygen reduction reaction by oxygen vacancies engineering, *Appl. Catal. B Environ.* 291 (2021), 120065, <https://doi.org/10.1016/j.apcatb.2021.120065>.
- [15] Y. Pei, Y.C. Ge, H. Chu, W. Smith, P. Dong, P.M. Ajayan, M.X. Ye, J.F. Shen, Controlled synthesis of 3D porous structured cobalt-iron based nanosheets by electrodeposition as asymmetric electrodes for ultra-efficient water splitting, *Appl. Catal. B Environ.* 244 (2019) 583–593, <https://doi.org/10.1016/j.apcatb.2018.11.091>.
- [16] X.H. Zhao, Z.M. Xue, W.J. Chen, X.Y. Bai, R.F. Shi, T.C. Mu, Ambient fast, large-scale synthesis of entropy-stabilized metal-organic framework nanosheets for electrocatalytic oxygen evolution, *J. Mater. Chem. A* 7 (2019) 26238–26242, <https://doi.org/10.1039/c9ta09975a>.
- [17] X.D. Cui, B.L. Zhang, C.Y. Zeng, S.M. Guo, Electrocatalytic activity of high-entropy alloys toward oxygen evolution reaction, *MRS Commun.* 8 (2018) 1230–1235, <https://doi.org/10.1557/mrc.2018.111>.
- [18] J. Lee, H. Jung, Y.S. Park, N. Kwon, S. Woo, N.C.S. Selvam, G.S. Han, H.S. Jung, P. J. Yoo, S.M. Choi, J.W. Han, B. Lim, Chemical transformation approach for high-performance ternary NiFeCo metal compound-based water splitting electrodes, *Appl. Catal. B Environ.* 294 (2021), 120246, <https://doi.org/10.1016/j.apcatb.2021.120246>.
- [19] K. Yao, Y. Xia, J. Li, N. Wang, J. Han, C. Gao, M. Han, G. Shen, Y. Liu, A. Seifitokaldani, X. Sun, H. Liang, Metal-organic framework derived copper catalysts for CO<sub>2</sub> to ethylene conversion, *J. Mater. Chem. A* 8 (2020) 11117–11123, <https://doi.org/10.1039/d0ta02395g>.
- [20] X. Wang, C. Liu, C. Gao, K. Yao, S.S.M. Masouleh, R. Berte, H. Ren, L.S. Menezes, E. Cortes, I.C. Bicket, H. Wang, N. Li, Z. Zhang, M. Li, W. Xie, Y. Yu, Y. Fang, S. Zhang, H. Xu, A. Vomiero, Y. Liu, G.A. Botton, S.A. Maier, H. Liang, Self-constructed multiple plasmonic hotspots on an individual fractal to amplify broadband hot electron generation, *ACS Nano* 15 (2021) 10553–10564, <https://doi.org/10.1021/acsnano.1c03218>.
- [21] X. Zhao, X.Q. Li, Y. Yan, Y.L. Xing, S.C. Lu, L.Y. Zhao, S.M. Zhou, Z.M. Peng, J. Zeng, Electrical and structural engineering of cobalt selenide nanosheets by Mn modulation for efficient oxygen evolution, *Appl. Catal. B-Environ.* 236 (2018) 569–575, <https://doi.org/10.1016/j.apcatb.2018.05.054>.
- [22] D.J. Zhou, Z. Cai, Y. Jia, X.Y. Xiong, Q.X. Xie, S.Y. Wang, Y. Zhang, W. Liu, H. H. Duan, X.M. Sun, Activating basal plane in NiFe layered double hydroxide by Mn<sup>2+</sup> doping for efficient and durable oxygen evolution reaction, *Nanoscale Horiz.* 3 (2018) 532–537, <https://doi.org/10.1039/c8nh00121a>.
- [23] Z.Y. Lv, X.J. Liu, B. Jia, H. Wang, Y. Wu, Z.P. Lu, Development of a novel high-entropy alloy with eminent efficiency of degrading azo dye solutions, *Sci. Rep.* 6 (2016) 34213, <https://doi.org/10.1038/srep34213>.
- [24] X. Bo, R.K. Hocking, S. Zhou, Y. Li, X. Chen, J. Zhuang, Y. Du, C. Zhao, Capturing the active sites of multimetallic (oxy)hydroxides for the oxygen evolution reaction, *Energy Environ. Sci.* 13 (2020) 4225–4237, <https://doi.org/10.1039/d0ee01609h>.
- [25] H. Liu, Y. Wang, X. Lu, Y. Hu, G. Zhu, R. Chen, L. Ma, H. Zhu, Z. Tie, J. Liu, Z. Jin, The effects of Al substitution and partial dissolution on ultrathin NiFeAl trinary layered double hydroxide nanosheets for oxygen evolution reaction in alkaline solution, *Nano Energy* 35 (2017) 350–357, <https://doi.org/10.1016/j.nanoen.2017.04.011>.
- [26] Y.P. Lin, H. Wang, C.K. Peng, L.M. Bu, C.L. Chiang, K. Tian, Y. Zhao, J.Q. Zhao, Y. G. Lin, J.M. Lee, L.J. Gao, Co-induced electronic optimization of hierarchical NiFe LDH for oxygen evolution, *Small* 16 (2020), 2002426, <https://doi.org/10.1002/smll.202002426>.
- [27] A.L. Wang, H. Xu, G.R. Li, NiCoFe layered triple hydroxides with porous structures as high-performance electrocatalysts for overall water splitting, *ACS Energy Lett.* 1 (2016) 445–453, <https://doi.org/10.1021/acsenergylett.6b00219>.
- [28] L. Yan, Y.R. Ren, X.L. Zhang, Y.L. Sun, J.Q. Ning, Y.J. Zhong, B.T. Teng, Y. Hu, Electronic modulation of composite electrocatalysts derived from layered NiFeMn triple hydroxide nanosheets for boosted overall water splitting, *Nanoscale* 11 (2019) 20797–20808, <https://doi.org/10.1039/c9nr07159h>.
- [29] G. Kresse, J. Furthmüller, Efficient iterative schemes for ab initio total-energy calculations using a plane-wave basis set, *Phys. Rev. B* 54 (1996) 11169–11186, <https://doi.org/10.1103/PhysRevB.54.11169>.
- [30] G. Kresse, D. Joubert, From ultrasoft pseudopotentials to the projector augmented-wave method, *Phys. Rev. B* 59 (1999) 1758–1775, <https://doi.org/10.1103/PhysRevB.59.1758>.
- [31] J.P. Perdew, K. Burke, M. Ernzerhof, Generalized gradient approximation made simple, 891–891, *Phys. Rev. Lett.* 80 (1998), <https://doi.org/10.1103/PhysRevLett.80.891>.
- [32] H.X. Xu, D.J. Cheng, D.P. Cao, X.C. Zeng, A universal principle for a rational design of single-atom electrocatalysts, *Nat. Catal.* 1 (2018) 339–348, <https://doi.org/10.1038/s41929-018-0063-z>.
- [33] S.L. Dudarev, G.A. Botton, S.Y. Savrasov, C.J. Humphreys, A.P. Sutton, Electron-energy-loss spectra and the structural stability of nickel oxide: an LSDA+U study, *Phys. Rev. B* 57 (1998) 1505–1509, <https://doi.org/10.1103/PhysRevB.57.1505>.
- [34] S. Grimme, Semiempirical GGA-type density functional constructed with a long-range dispersion correction, *J. Comput. Chem.* 27 (2006) 1787–1799, <https://doi.org/10.1002/jcc.20495>.

- [35] J.K. Norskov, J. Rossmeisl, A. Logadottir, L. Lindqvist, J.R. Kitchin, T. Bligaard, H. Jonsson, Origin of the overpotential for oxygen reduction at a fuel-cell cathode, *J. Phys. Chem. B* 108 (2004) 17886–17892, <https://doi.org/10.1021/jp047349j>.
- [36] Z.Y. Lu, L. Qian, Y. Tian, Y.P. Li, X.M. Sun, X. Duan, Ternary NiFeMn layered double hydroxides as highly-efficient oxygen evolution catalysts, *Chem. Commun.* 52 (2016) 908–911, <https://doi.org/10.1039/c5cc08845c>.
- [37] L. Xu, Q.Q. Jiang, Z.H. Xiao, X.Y. Li, J. Huo, S.Y. Wang, L.M. Dai, Plasma-engraved  $\text{Co}_3\text{O}_4$  nanosheets with oxygen vacancies and high surface area for the oxygen evolution reaction, *Angew. Chem. Int. Ed.* 55 (2016) 5277–5281, <https://doi.org/10.1002/anie.201600687>.
- [38] H.J. Qiu, G. Fang, J.J. Gao, Y.R. Wen, J. Lv, H.L. Li, G.Q. Xie, X.J. Liu, S.H. Sun, Noble metal-free nanoporous high-entropy alloys as highly efficient electrocatalysts for oxygen evolution reaction, *ACS Mater. Lett.* 1 (2019) 526–533, <https://doi.org/10.1021/acsmaterialslett.9b00414>.
- [39] O. Diaz-Morales, D. Ferrus-Suspiedra, M.T.M. Koper, The importance of nickel oxyhydroxide deprotonation on its activity towards electrochemical water oxidation, *Chem. Sci.* 7 (2016) 2639–2645, <https://doi.org/10.1039/c5sc04486c>.
- [40] S. Anantharaj, S. Kundu, Do the evaluation parameters reflect intrinsic activity of electrocatalysts in electrochemical water splitting? *ACS Energy Lett.* 4 (2019) 1260–1264, <https://doi.org/10.1021/acsenergylett.9b00686>.
- [41] L. Zhang, W. Cai, N. Bao, Top-level design strategy to construct an advanced high-entropy Co-Cu-Fe-Mo (oxy)hydroxide electrocatalyst for the oxygen evolution reaction, *Adv. Mater.* 33 (2021), 2100745, <https://doi.org/10.1002/adma.202100745>.
- [42] H. Qiao, X. Wang, Q. Dong, H. Zheng, G. Chen, M. Hong, C.P. Yang, M. Wu, K. He, L. Hu, A high-entropy phosphate catalyst for oxygen evolution reaction, *Nano Energy* 86 (2021), 106029, <https://doi.org/10.1016/j.nanoen.2021.106029>.
- [43] T.X. Nguyen, Y.H. Su, C.C. Lin, J. Ruan, J.M. Ting, A new high entropy glycerate for high performance oxygen evolution reaction, *Adv. Sci.* 8 (2021), 2002446, <https://doi.org/10.1002/advs.202002446>.
- [44] J. Tang, J.L. Xu, Z.G. Ye, X.B. Li, J.M. Luo, Microwave sintered porous  $\text{CoCrFeNiMo}$  high entropy alloy as an efficient electrocatalyst for alkaline oxygen evolution reaction, *J. Mater. Sci. Technol.* 79 (2021) 171–177, <https://doi.org/10.1016/j.jmst.2020.10.079>.
- [45] M.J. Cui, C.P. Yang, B.Y. Li, Q. Dong, M.L. Wu, S. Hwang, H. Xie, X.Z. Wang, G. F. Wang, L.B. Hu, Sulprostone-induced gastric dysrhythmia in the ferret: conventional and advanced analytical approaches, *Front. Physiol.* 11 (2020), 583082, <https://doi.org/10.1002/aenm.202002887>.
- [46] T. Wang, H. Chen, Z.Z. Yang, J.Y. Liang, S. Dai, High-entropy perovskite fluorides: a new platform for oxygen evolution catalysis, *J. Am. Chem. Soc.* 142 (2020) 4550–4554, <https://doi.org/10.1021/jacs.9b12377>.
- [47] K. Huang, B.W. Zhang, J.S. Wu, T.Y. Zhang, D.D. Peng, X. Cao, Z. Zhang, Z. Li, Y. Z. Huang, Exploring the impact of atomic lattice deformation on oxygen evolution reactions based on a sub-5 nm pure face-centred cubic high-entropy alloy electrocatalyst, *J. Mater. Chem. A* 8 (2020) 11938–11947, <https://doi.org/10.1039/d0ta02125c>.
- [48] M.W. Glasscott, A.D. Pendergast, S. Goines, A.R. Bishop, A.T. Hoang, C. Renault, J. E. Dick, Electrosynthesis of high-entropy metallic glass nanoparticles for designer, multi-functional electrocatalysis, *Nat. Commun.* 10 (2019) 2650, <https://doi.org/10.1038/s41467-019-10303-z>.
- [49] Z.Y. Jin, J. Lv, H.L. Jia, W.H. Liu, H.L. Li, Z.H. Chen, X. Lin, G.Q. Xie, X.J. Liu, S. H. Sun, H.J. Qiu, Nanoporous Al-Ni-Co-Ir-Mo high-entropy alloy for record-high water splitting activity in acidic environments, *Small* 15 (2019), 1904180, <https://doi.org/10.1002/smll.201904180>.
- [50] W.J. Liu, X. Hu, H.C. Li, H.Q. Yu, Pseudocapacitive Ni-Co-Fe hydroxides/N-doped carbon nanoplates-based electrocatalyst for efficient oxygen evolution, *Small* 14 (2018), 1801878, <https://doi.org/10.1002/smll.201801878>.
- [51] X. Zhao, Z. Xue, W. Chen, Y. Wang, T. Mu, Eutectic synthesis of high-entropy metal phosphides for electrocatalytic water splitting, *ChemSusChem* 13 (2020) 2038–2042, <https://doi.org/10.1002/cssc.202000173>.
- [52] X. Bo, Y.B. Li, R.K. Hocking, C. Zhao, NiFeCe hydroxide holey nanosheet as advanced electrocatalyst for water oxidation, *ACS Appl. Mater. Interfaces* 9 (2017) 41239–41245, <https://doi.org/10.1021/acsmami.7b12629>.
- [53] M.W. Louie, A.T. Bell, An investigation of thin-film Ni-Fe oxide catalysts for the electrochemical evolution of oxygen, *J. Am. Chem. Soc.* 135 (2013) 12329–12337, <https://doi.org/10.1021/ja405351s>.
- [54] S. Klaus, Y. Cai, M.W. Louie, L. Trotochaud, A.T. Bell, Effects of Fe electrolyte impurities on  $\text{Ni}(\text{OH})(\text{O})/\text{NiOOH}$  structure and oxygen evolution activity, *J. Phys. Chem. C* 119 (2015) 7243–7254, <https://doi.org/10.1021/acs.jpcc.5b00105>.
- [55] J. Mohammed-Ibrahim, A review on NiFe-based electrocatalysts for efficient alkaline oxygen evolution reaction, *J. Power Sources* 448 (2020), 227375, <https://doi.org/10.1016/j.jpowsour.2019.227375>.